The Astrophysical Journal, 705:144–155, 2009 November 1 doi:10.1088/0004-637X/705/1/144

MOLECULAR AND ATOMIC GAS IN THE LARGE MAGELLANIC CLOUD. II. THREE-DIMENSIONAL CORRELATION BETWEEN CO AND H I

Y. Fukui[1], A. Kawamura[1], T. Wong[2], M. Murai[1], H. Iritani[1], N. Mizuno[1,3], Y. Mizuno[1], T. Onishi[1,4], A. Hughes[5,6], J. Ott[7,8], E. Muller[1], L. Staveley-Smith[9], and S. Kim[10]

[1] Department of Astrophysics, Nagoya University, Furocho, Chikusaku, Nagoya 464-8602, Japan; fukui@a.phys.nagoya-u.ac.jp, kawamura@a.phys.nagoya-u.ac.jp
[2] Astronomy Department, University of Illinois, 1002 W. Green Street, Urbana, IL 61801, USA
[3] National Astronomical Observatory of Japan, 2-21-1 Osawa, Mitaka, Tokyo 181-8588, Japan
[4] Department of Physical Science, Osaka Prefecture University, Gakuen 1-1, Sakai, Osaka 599-8531, Japan
[5] Centre for Astrophysics and Supercomputing, Swinburne University of Technology, P.O. Box 218, Hawthorn, VIC 3122, Australia
[6] CSIRO Australia Telescope National Facility, P.O. Box 76, Epping, NSW 1710, Australia
[7] National Radio Astronomy Observatory, 520 Edgemont Road, Charlottesville, VA 22903, USA
[8] California Institute of Technology, MC 10524, Pasadena, CA 91125, USA
[9] School of Physics M013, University of Western Australia, Crawley, WA 6009, Australia
[10] Department of Astronomy and Space Science, Sejong University, KwangJin-gu, KunJa-dong 98, Seoul 143-747, Korea
Received 2008 December 19; accepted 2009 September 3; published 2009 October 8

ABSTRACT

We compare the CO ($J = 1$–0) and H I emission in the Large Magellanic Cloud in three dimensions, i.e., including a velocity axis in addition to the two spatial axes, with the aim of elucidating the physical connection between giant molecular clouds (GMCs) and their surrounding H I gas. The CO $J = 1$–0 data set is from the second NANTEN CO survey and the H I data set is from the merged Australia Telescope Compact Array (ATCA) and Parkes Telescope surveys. The major findings of our analysis are as follows: (1) GMCs are associated with an envelope of H I emission, (2) in GMCs [average CO intensity] $\propto$ [average H I intensity]$^{1.1\pm0.1}$, and (3) the H I intensity tends to increase with the star formation activity within GMCs, from Type I to Type III. An analysis of the H I envelopes associated with GMCs shows that their average line width is 14 km s^{-1} and the mean density in the envelope is 10 cm^{-3}. We argue that the H I envelopes are gravitationally bound by GMCs. These findings are consistent with a continual increase in the mass of GMCs via H I accretion at an accretion rate of 0.05 $M_{\odot}$ yr^{-1} over a timescale of 10 Myr. The growth of GMCs is terminated via dissipative ionization and/or stellar-wind disruption in the final stage of GMC evolution.

Key words: galaxies: ISM – ISM: atoms – ISM: clouds – ISM: molecules – Magellanic Clouds – radio lines: ISM

Online-only material: color figures

1. INTRODUCTION

Giant molecular clouds (GMCs), the most massive aggregations of interstellar matter with 10^5–10^6 $M_{\odot}$, are the principal sites of star formation in galaxies. It is important to understand how GMCs are formed out of the less dense atomic interstellar gas in order to understand galactic evolution. The interstellar H I gas has densities of less than several 10 cm^{-3}, while molecular clouds have densities larger than 100 cm^{-3}. It is reasonable to assume that H I is being converted into H_2 either by thermal/gravitational instabilities and/or shock compressions, although the detailed processes of this conversion are not yet well understood. Sato & Fukui (1978) and Hasegawa et al. (1983) identified cold H I gas associated with GMCs in M17 and W3/4 and suggested that the cold H I gas may be converted into molecular gas for these GMCs. Subsequently, Wannier et al. (1983) showed that five molecular clouds are associated with warm H I envelopes and suggested that such H I envelopes may be common around GMCs. Nonetheless, associations between GMCs and H I envelopes are difficult to identify systematically throughout the Galactic disk, since GMC samples are restricted to the solar vicinity due to the crowding effects (Andersson et al. 1991). As a consequence, the GMC–H I association has not been well established.

The Magellanic system—including the Large Magellanic Cloud (LMC), the Small Magellanic Cloud (SMC), and the Bridge—is an ideal laboratory to study star formation and molecular cloud evolution because of its proximity to the Milky Way (e.g., Fukui et al. 1999, 2008; Mizuno et al. 2001, 2006; Ott et al. 2008; Kawamura et al. 2009). We expect that the Magellanic system can also shed light on the physical connection between GMCs and their atomic surroundings. Indeed, the LMC may offer the best place for such a study because of its nearly face-on orientation and level of star formation activity. The LMC's molecular cloud population, which is best traced via the CO emission, provides a key to understand the galaxy's star formation. Molecular clouds are able to highlight the location of star formation due to their highly clumped distribution in both space and velocity. The LMC's atomic gas, by contrast, has lower densities and is only weakly coupled to sites of active star formation, but it is the most promising candidate for the mass reservoir of GMC formation (e.g., Blitz et al. 2007). We note, moreover, that cold H I gas has been detected in the LMC (e.g., Dickey et al. 1994; Kim et al. 1999), and that the correlation between CO and H I may provide crucial observational evidence about the molecular cloud formation process.

Wong et al. (2009) compared the H I and CO emission throughout the LMC on a pixel-by-pixel basis using the second NANTEN CO and ATCA+Parkes H I data sets. These authors studied correlations between the integrated CO and H I intensities, where the latter was integrated over all velocities with H I emission or over individual Gaussian components. They found that CO emission is associated with high intensity H I gas but that intense H I emission is not always associated with CO.

Table 1
Physical Properties of GMCs

GMC Type	Number of GMCs	M_{CO}[a] ($\times 10^5\ M_\odot$)	R[a] (pc)	N(H I)[b] ($\times 10^{21}$ cm $^{-2}$)	ΔV_{LSR} (H I)[b] (km s^{-1})	ΔV_{LSR} (CO)[a] (km s^{-1})
Type I	72	2 (2)	37 (16)	···	···	5.0 (2.5)
Type II	142	2 (3)	33 (19)	···	···	4.8 (2.2)
Type III	58	5 (10)	51 (36)	···	···	6.9 (3.0)
Type I (selected)[c]	24	2 (3)	35 (17)	2.4 (0.9)	13.9 (4.0)	4.5 (2.1)
Type II (selected)[c]	67	2 (3)	41 (22)	2.6 (1.2)	14.6 (4.1)	4.4 (1.6)
Type III (selected)[c]	32	4 (3)	55 (23)	3.3 (1.5)	16.1 (3.3)	5.5 (1.5)

Notes. Average properties of the GMCs. The values in parentheses are the standard deviation.
[a] Fukui et al. (2008); Kawamura et al. (2009).
[b] Half-intensity full width derived by Gaussian fitting.
[c] Selected clouds having single-peaked H I profiles.

They also discovered a weak tendency for CO to be associated with H I components that have relatively low velocity dispersion. This suggests that energy dissipation of the H I gas may be required for the formation of molecular clouds. Following the global analysis by Wong et al. (2009), we focus here on the H I associated with individual GMCs in the LMC. In order to address this issue, we conduct a detailed comparison between the CO and H I emission in three dimensions, i.e., (x, y, v), at a spatial resolution of ∼40 pc and a velocity resolution of 1.7 km s^{-1}. The present study is complementary to the work by Wong et al. (2009); in conjunction, the two studies provide a new insight into the CO–H I connection. In Section 2, we briefly review the basic observational properties of GMCs in the LMC. In Section 3, we describe our method of analyzing the CO–H I correlation and present our results. We discuss the physical interpretation of our results in Section 4, and provide a summary of our major conclusions in Section 5.

2. GMCs IN THE LMC: THE SECOND NANTEN CO SURVEY

The LMC is extended by more than 30 deg^2 across the sky and it has been a difficult task to make a systematic survey of the CO emission at angular resolutions sufficient to resolve individual GMCs. Fukui et al. (1999) made such a survey in the 2.6 mm CO line with the NANTEN 4 m mm-wave telescope and published the first results in Fukui et al. (1999). Subsequently, these authors completed another survey of the LMC, improving the sensitivity by a factor of 2. The second NANTEN CO survey has cataloged 272 GMCs (Fukui et al. 2008). The basic physical parameters of GMCs in the LMC are similar to those in the Milky Way and other nearby galaxies. Their masses range from $\sim 10^5\ M_\odot$ to $\sim 10^6\ M_\odot$; the mass spectrum is quite steep with a slope of $dN/dM \sim M^{-2}$. The X factor, the ratio of the H_2 column density to CO intensity, is $\sim 7 \times 10^{20}$ cm^{-2} (K km s^{-1}) $^{-1}$ (Fukui et al. 2008; Blitz et al. 2007). The complete sampling of the NANTEN survey has also allowed us to make a statistical study of GMCs with various young objects including H II regions and young stellar clusters. Kawamura et al. (2009) confirmed that there are three classes of GMCs that can be categorized according to their association with young star clusters as originally indicated in the analysis of the first NANTEN LMC survey (Fukui et al. 1999; Yamaguchi et al. 2001). Type I GMCs show no signs of active star formation in the sense that no O stars are being formed. Type II GMCs are associated with small H II region(s), indicating the formation of isolated O stars, but do not host any stellar clusters identified by Bica et al. (1996). Type III GMCs are actively forming stars as shown by their association with large H II regions and young stellar clusters. These classes are interpreted as an evolutionary sequence from Type I to III; the lifetime of a GMC is estimated to be a few ×10 Myr in total (Kawamura et al. 2009). The stage after Type III is likely to be a very violent dissipation of the GMC due to the UV photons and stellar winds produced by the nascent clusters, as seen spectacularly in the region of 30 Dor (Yamaguchi et al. 2001). A comparison of the physical parameters of the GMCs shows that the size and mass of the clouds tend to increase from Type I/II to Type III. A summary of the average mass and size for the three GMC classes is presented in Table 1, as taken from Kawamura et al. (2009).

3. CORRELATION BETWEEN CO AND H I

3.1. Three-dimensional Correlation

Previous studies of star formation in galaxies have employed two-dimensional (2D) maps of H I intensity with large spatial averaging on scales between ∼100 pc and 1 kpc (e.g., Schmidt 1972; Kennicutt 1998). Here, we make a three-dimensional (3D) comparison between the CO and H I in the LMC where the 3D datacubes have a velocity axis in addition to two spatial axes projected on the sky. Preliminary results of the comparison have been published elsewhere (Fukui 2007). We use the 3D datacube of CO obtained with NANTEN (Fukui et al. 2008) and an H I datacube obtained with ATCA and Parkes (Kim et al. 2003). The CO emission traces GMCs and the H I emission traces less dense atomic gas. Figure 1 shows an overlay of the velocity-integrated intensities of the CO and H I emission; from this, it is clear that GMCs in the LMC tend to be located toward H I filaments or local H I peaks, suggesting that H I is a prerequisite for GMC formation (Blitz et al. 2007). However, it is also clear that there are many H I peaks and filaments without CO emission (Wong et al. 2009). Figure 2 shows typical CO and H I line profiles in the LMC. The CO emission is highly localized in velocity: the H I emission ranges over 100 km s^{-1}, while the CO emission has a typical line width of less than 10 km s^{-1}. We note that the large velocity dispersion of H I may be dominated by physically unrelated velocity components along the line of sight, i.e., the H I gas associated with the GMC may only be the small fraction of H I with velocities close to that of the CO emission. Previous studies of the CO–H I connection that use velocity-integrated 2D maps may therefore overestimate the intensity of the associated H I emission along each line of sight. By making use of the velocity dimension, the present 3D analysis may allow us to identify the H I gas that is physically connected to the GMCs. The NANTEN and

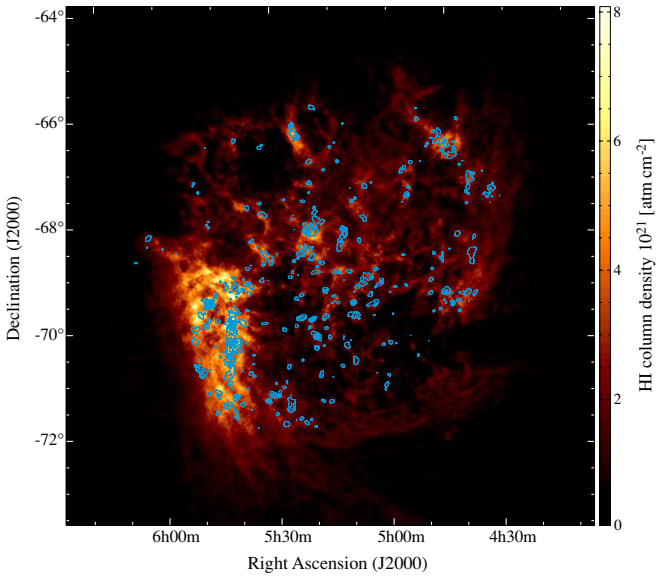

Figure 1. H I integrated intensity image (Kim et al. 2003) with contours of the CO integrated intensity (Fukui et al. 2008). The contour levels begin at 1.2 K km s^{-1} and have 3.6 K km s^{-1} intervals.

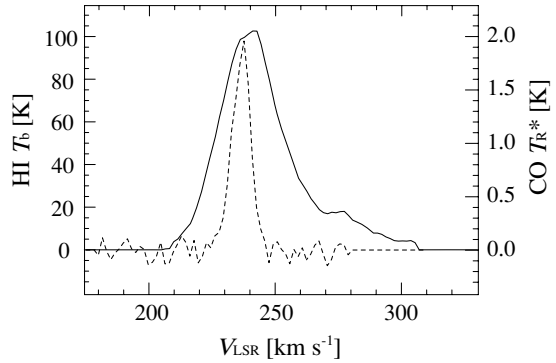

Figure 2. Example of the H I and CO line profiles at α(J2000) = $5^h39^m38^s$ and δ(J2000) = $-69°44'46''$.

ATCA+Parkes datacubes have somewhat different spatial and velocity resolutions, so we have convolved both data sets to a spatial resolution of 40 pc × 40 pc, and a velocity resolution of 1.7 km s^{-1}. The total number of 3D pixels is approximately 2×10^6 across the area surveyed by NANTEN. The H I and CO intensities are expressed in units of T_b (K) and T_R^* (K); the 3σ noise levels of the H I and CO datacubes are 7.2 K and 0.21 K, respectively. Strictly speaking, the one-to-one correspondence between a velocity and a position is not guaranteed because there is a chance that physically unrelated H I gas may have the same velocity as H I gas related to the GMC along the same line of sight. Our results identify the H I associated with GMCs and suggest that such contamination along individual sightlines may not be a serious problem. We further note that H I absorption toward background radio continuum sources does not affect significantly the H I intensity at the present spatial resolution, as verified toward 30 Dor, one of the brightest radio continuum sources in the LMC.

Figure 3 shows a histogram of the H I intensity in the 3D datacube. Pixels with the significant CO emission ($T_R^* > 0.21$ K) are shown in red. Throughout this paper, histograms always use the values of 3D pixels with no spatial integration unless otherwise stated. The histogram in Figure 3 shows that the fraction of CO-detected pixels increases monotonically with the

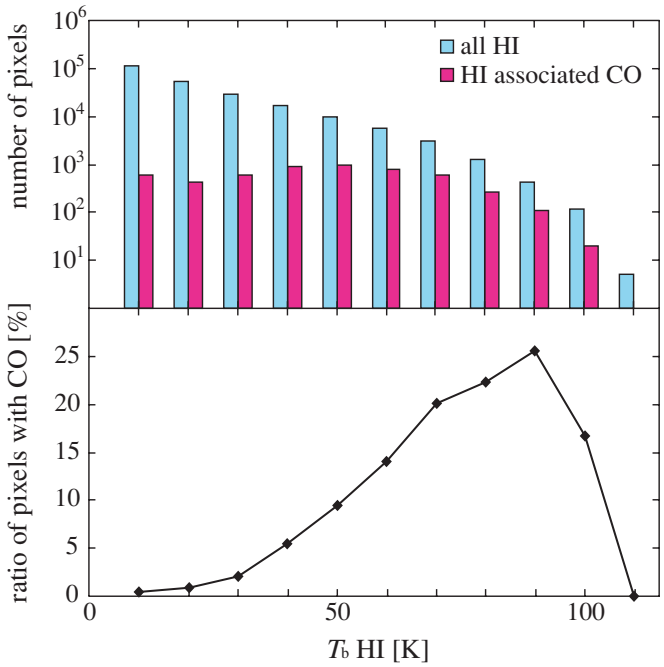

Figure 3. H I and CO datacubes used for our analysis have somewhat different spatial and velocity resolutions; we have convolved both data sets to a spatial resolution of 40 pc × 40 pc, and a velocity resolution of ×1.7 km s^{-1} across the whole LMC. The pixels used in our analysis occupy the same volumes for both the H I and CO data sets. The 3σ detection limits for the CO and H I brightness are 0.21 K and 7.2 K, respectively. (a) Histogram of the H I brightness temperature averaged within each 3D pixel is shown in blue; the H I pixels with significant CO emission (i.e., > 3σ) are marked in red. The width of the histogram bins is 10 K. (b) Ratio of the number of pixels with significant H I emission to those with significant CO emission within each 10 K bin.

H I intensity, suggesting the H I intensity is a necessary condition to form GMCs, consistent with the conclusion by Wong et al. (2009). About one-third of the pixels with T_b(H I) of ∼90 K exhibit CO emission, but it seems that there is no sharp threshold value of H I intensity that is required for GMC formation.

Figure 4 shows a histogram of the H I intensity for the three GMC types. Each pixel detected in CO belongs to one of the GMCs cataloged in Fukui et al. (2008). Figure 4 clearly shows that the H I intensity tends to increase from Type I to Type III, although the dispersion is considerable. The average H I intensity for Types I, II, and III GMCs across the LMC is 34 ± 16 K (1σ), 47 ± 17 K, and 56 ± 19 K, i.e., the average H I intensity increases with the level of star formation activity within the GMC. In order to test for variation within the galaxy, we tentatively divide the galaxy into three regions, i.e., Bar, North, and Arc, as shown in Figure 4 (right). Histograms for each region, shown in the lower three panels of Figure 4, reveal the same trend, suggesting that the present trend is common over the whole LMC. The total number of pixels in each region is 429,510, 666,060, and 405,093. Type I, Type II, and Type III GMCs include 330, 1065, and 639 pixels in the Bar region; 346, 878, and 1158 pixels in the North region; and 389, 650, and 1231 pixels in the Arc region.

Figure 5 shows the velocity channel maps of the H I distribution associated with Type I, Type II, and Type III GMCs. These channel maps clearly show that the H I is associated with the CO. The CO distribution has small structures of ∼100 pc or less and the H I appears to be associated with the GMC on larger scales of ∼100 to 400 pc. The H I emission is not always symmetric with respect to a GMC, even though H I typically

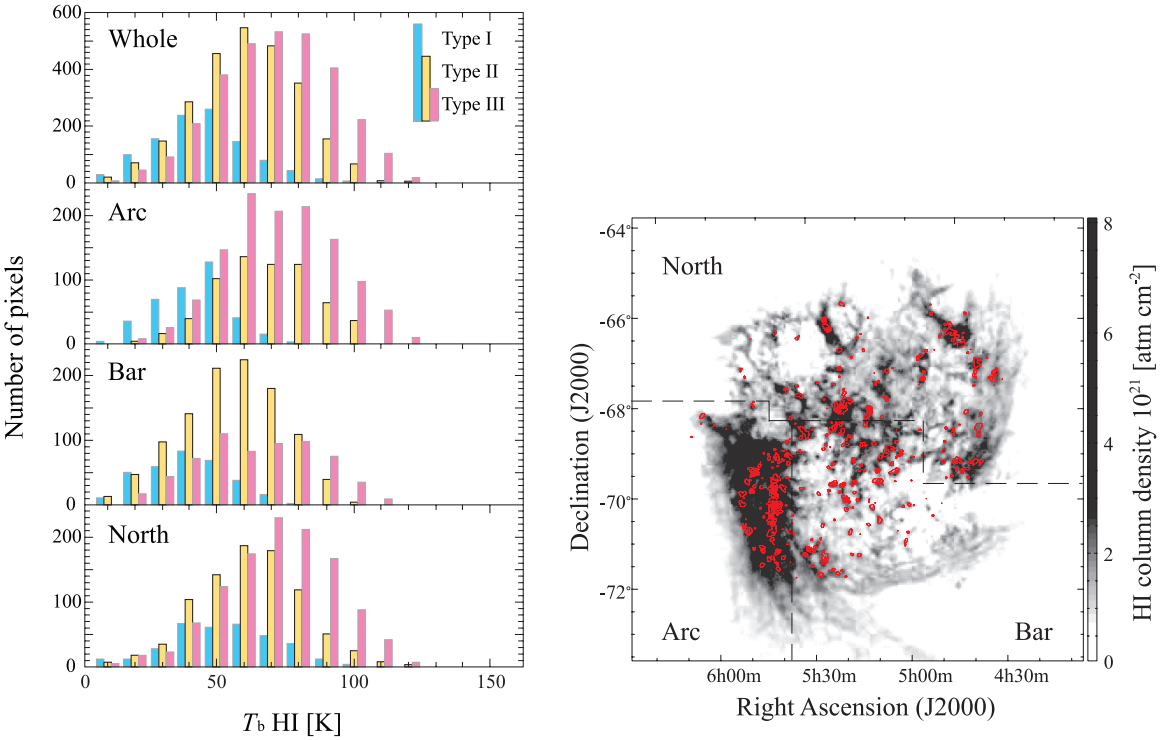

Figure 4. Histograms of the pixel-averaged H I brightness temperature where significant CO emission is detected for Type I (blue), Type II (yellow), and Type III (red) GMCs. Histograms are shown for the whole LMC, and for three different regions—Bar, North, and Arc—which are indicated in the right panel.
(A color version of this figure is available in the online journal.)

envelopes each GMC. The associated H I is often elongated along the GMCs and the region of intense H I emission is usually <100 pc wide. The CO emission typically extends over a velocity range of ∼5 km s^{-1}; beyond a few times this velocity range, the associated H I emission generally becomes much weaker or disappears.

3.2. Physical Properties of the H I Envelope

In general, it is a complicated task to derive reliable physical properties of the H I gas associated with a GMC because the H I profiles are a blend of several different components along the line of sight, making it difficult to select the H I gas that is physically connected to a GMC. Another obstacle is that the H I emission is spatially more extended than the CO emission and has a less clear boundary than the CO.

For our analysis, we first selected GMCs with simple single-peaked H I profiles from the Fukui et al. (2008) catalog. The resulting sample consists of 123 GMCs in total. Their catalog numbers and basic physical properties, taken from Fukui et al. (2008), are listed in Table 2. For these GMCs, we tested whether there was a bias in their location with respect to the kinematic center of the galaxy, in their CO line width or in their molecular mass. The histograms in Figure 6 indicate that there is no particular trend for these properties of the selected GMCs compared to GMCs in the complete catalog, suggesting that there is no appreciable selection bias. We applied a Kolmogorov–Smirnov test to the three histograms and calculated maximum deviations of 0.031, 0.061, and 0.117, respectively, for the three parameters. These values are less than the critical deviation, 0.129, for a conventional significance level of 0.05, confirming that there is no selection bias.

Next, we made Gaussian fits to the H I and CO profiles toward the CO peak of each GMC. This procedure yields a peak intensity, peak velocity, and half-power line width for each line profile (a summary is given for each GMC type in Table 1). Figure 7 shows the relation between the CO line width and the difference between the CO and H I peak velocities. We find the H I and CO peak velocities to be in good agreement, showing only a small scatter of less than a few km s^{-1}. Figure 8 shows two histograms of the H I and CO line widths. We see that the H I line width is typically 14 km s^{-1}, roughly three times larger than that of CO. Figure 9 shows a correlation between H I and CO line widths. The two quantities show a positive correlation with a correlation coefficient of 0.39. The correlation coefficient is determined using the Spearman rank method throughout this paper. The kinematic properties of H I and CO, as illustrated in Figures 7 and 9, lend further support to a physical association between the H I and CO.

In order to estimate the size of the H I envelope surrounding each GMC, we construct an H I integrated intensity map of each GMC. First, we find the local peak in the H I intensity cube surrounding the CO emission, and then integrate the H I intensity over the velocity channels corresponding to the FWHM of the H I line profile at this peak position. Next we estimate the area, S, where the H I integrated intensity is greater than 80% of the value at the local H I peak. We then calculate the radius of the H I envelope, R(H I), from its projected area, $S = \pi R(\mathrm{H\,I})^2$. The H I integrated intensity is calculated for all the pixels with detectable CO emission; the spatial distribution of the H I emission generally shows a peak and a reasonably defined boundary. The 80% level was chosen after a few trials using different levels; it is the maximum value for which a reasonable H I size is obtained for 116 of the 123 envelopes. While 80% seems to be rather high for such a definition of a cloud envelope, the H I size can be unrealistically large compared to the CO cloud size along a filamentary H I distribution if we use a lower

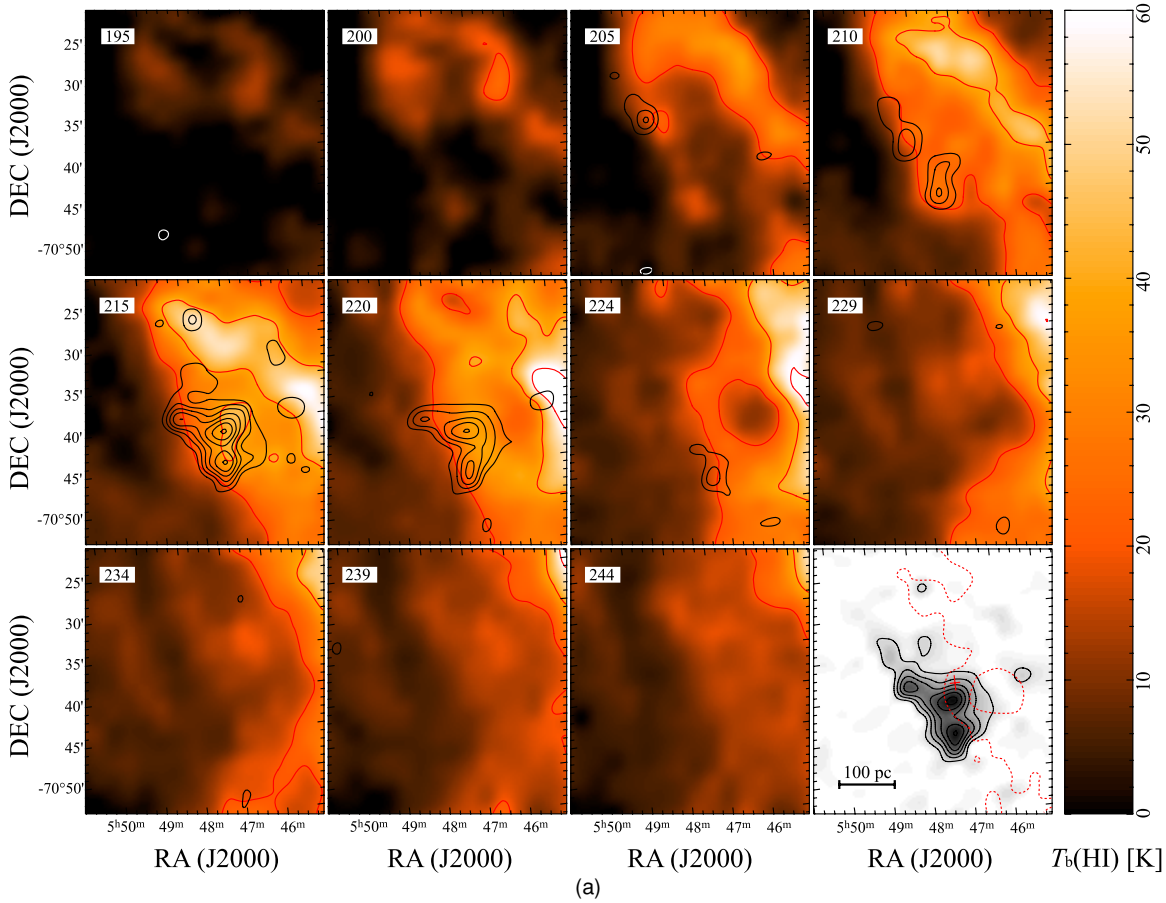

Figure 5. Velocity channel maps of the H I and CO emission associated with Type I, Type II, and Type III GMCs. The gray-scale images with black contours are H I brightness temperature (Kim et al. 2003) and the white contours are CO intensity (Fukui et al. 2008). The central velocity of the included channels is shown in the upper left of each panel. The lower right panel of each figure shows the total CO integrated intensity. The red contours and the red cross in the lower right panel of (a) and (b) present the 80% level of the H I peak intensity and the position of the H I intensity peak, respectively. (a) GMC No. 225 in the NANTEN catalog. CO contour levels are from 0.105 K km s^{-1} (3σ) with 0.105 K km s^{-1} intervals. H I contour levels are from 20 K with 20 K intervals. This is a case where the 80% level of the H I peak intensity is very extended relative to the size of the GMC. (b) GMC No. 134 and 135 between LMC4 and LMC5. CO integrated intensities are from 0.105 K km s^{-1} with 0.105 K km s^{-1} intervals. H I contour levels are from 20 K with 20 K intervals. This is a case where the 80% of the H I peak intensity provides a sensible definition of the H I envelope size. (c) GMC No. 192 and 202 with the H II region N159. CO integrated intensities are from 0.105 K km s^{-1} with 0.21 K km s^{-1} (6σ) intervals. H I contour levels are from 20 K with 20 K intervals. This is a region where the H I emission is very complicated; it was not selected in the sample of 123 clouds that we use for our analysis.

level such as 60%; an example is shown in Figure 5(b). The H I radius is then corrected for beam dilution by adopting Gaussian deconvolution with an H I FWHM of 2.6 arcmin, i.e., the same procedure that is applied to the radius of the GMC determined from the CO emission, R(CO) (Kawamura et al. 2009). R(CO), the CO peak position, R(H I), the H I peak position, and the deviation between the peaks in parsecs, $\sqrt{(\Delta\alpha^2 + \Delta\delta^2)}$, are listed in Table 2. Seven clouds, for which R(H I) comprises only a few pixels, are denoted by asterisks. The physical extent of the H I envelopes can be as large as a few 100 pc. As long as we use the local H I peak of individual GMCs as our reference point, it seems difficult to contrive an alternative uniform definition of the envelope size that is difficult using the present H I data set.

In Figure 10, we show a histogram of the spatial deviation of the H I and CO peaks. This shows that nearly 80% of the H I envelopes peak within 120 pc of the local CO peak, and that nearly 60% of the H I envelopes peak within 80 pc of the CO peak. These separations may seem large compared to R(H I), but we argue that they are reasonable if the H I is enveloping CO at scales over ~300 pc. It should be noted that the H I envelopes are not concentric with the CO emission, but are rather "enveloping" with some offsets in peak positions as illustrated in Figure 5. We thus expect to find some difference in general between the peak positions of the CO and H I emission (as seen in Figure 10), but the fact that the majority of H I peaks are located within 120 pc of the CO peaks is clearly suggestive of a physical association between the GMCs and their surrounding atomic gas. In Figure 11, we show a correlation between R(H I) and R(CO) for 62 GMCs whose radius is greater than 30 pc and find that they are positively correlated with a correlation coefficient of 0.45. Despite the relatively flatter distribution of the H I, the size of the H I envelope does seem to correlate with the size of the GMC.

To summarize our analysis in this section, we find for the 123 GMCs with single-peaked H I profiles that (1) the peak velocities of the CO and H I are in good agreement (Figure 7); (2) the CO and H I line widths show a positive correlation (Figure 9); (3) the H I envelopes, defined using the 80% level of the local H I integrated intensity peak, are mostly (~80%) centered within 120 pc of the peak CO position (Figure 10); and (4) the radius of the H I envelope is positively correlated with the size of the GMC for GMCs with radii greater than 30 pc (Figure 11). These four results lend further support to the idea that H I envelopes are physically associated with GMCs, reinforcing the impression

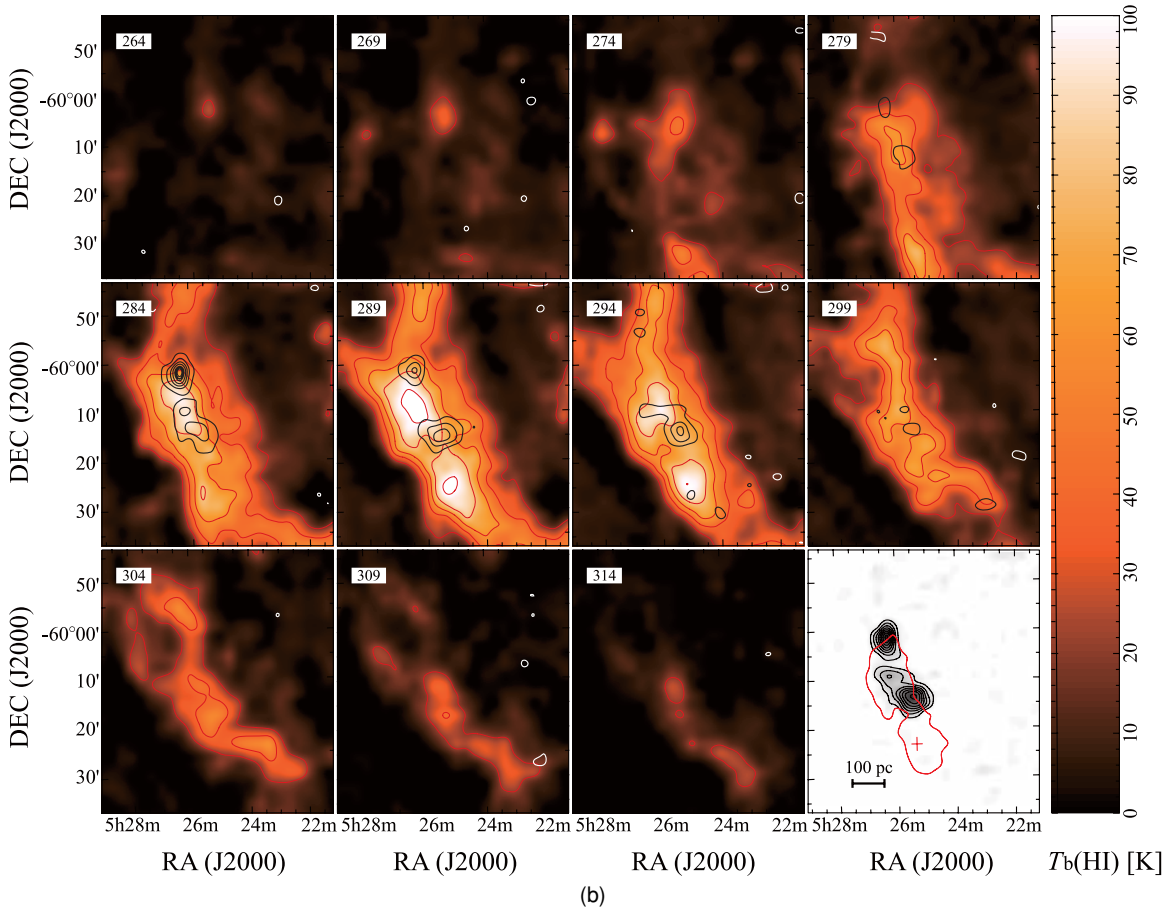

Figure 5. (Continued)

conveyed by a global comparison between the H I CO emission in the LMC (Figure 3) and the morphological similarity between the CO and H I in individual velocity channels (Figure 5).

Next, we made an estimate of the H I column density for the 123 GMCs by using the relation (N (H I) [cm^{-2}] = $1.8 \times 10^{18} \int T_b dv$ [K km s^{-1}]). The average values for the three GMC types are listed in Table 1. We find that the peak H I column density is mostly in the range of (2–5) $\times 10^{21}$ cm^{-2}. We estimate the typical density in the H I envelopes to be $\sim$10 cm^{-1} by dividing the peak H I column density (2–5) $\times 10^{21}$ cm^{-2} by the typical size of the associated H I 50–100 pc (see Figure 11). The mass of the H I envelopes is large, typically $\sim 5 \times 10^4$ $M_\odot$. The H I envelopes are likely gravitationally bound by GMCs because one-half of the H I line width, 7 km s^{-1}, is nearly equal to $\sqrt{GM/R} \sim 6$ km s^{-1} for $M = 2 \times 10^5$ $M_\odot$ and $R = 40$ pc, the average values of Type II GMCs.

In Figure 12, we plot the relationship between the average CO and H I luminosity of the 123 GMCs. For each GMC, we selected pixels where CO emission is significantly detected: only these pixels are used to calculate the H I luminosity of each cloud. In order to derive the average CO luminosity of a GMC, we estimated I(CO) (K km s^{-1}) by summing up the CO luminosity over all the pixels of a GMC and divide it by the area of the GMC. I(H I) (K km s^{-1}) is calculated in a similar manner, integrating the H I intensity over the FWHM velocity range at the CO peak of the GMC. The regression shown in Figure 12 is well fitted by a power law with an index of $\sim$1.1, indicating a nearly linear correlation between I(CO) and I(H I) in a GMC.

4. DISCUSSION

4.1. GMCs with H I Envelopes

The present analysis has successfully identified the H I envelopes associated with GMCs on the basis of a 3D analysis of GMCs in the LMC. The H I intensity in the envelope depends on the star-forming activity within the GMC in the sense that the integrated H I intensity in the envelope increases from Type I to Type III (Figure 4, Section 3.1). In other words, massive GMCs have massive H I envelopes and less massive GMCs have less massive H I envelopes.

The H I intensity is a product of the spin temperature and the optical depth of the H I 21 cm transition, provided that the line is optically thin. This is likely to be the case as the H I profiles show few hints of saturation like a flat top. The observed maximum H I brightness temperature is around 100 K and this suggests that the H I spin temperature is significantly higher than 100 K. Therefore, we infer that the H I intensity should represent optical depth and, accordingly, H I column density, if the spin temperature is roughly uniform across the LMC. The H I spin temperature in the LMC may be higher than in the Galaxy due to a more intense UV field and the lower dust extinction (Israel et al. 1996; Imara & Blitz 2007; Dobashi et al. 2008). For the sake of discussion, we shall tentatively assume that the spin temperature lies between 150 and 600 K and is fairly uniform in the H I envelope. We note that the H I mass is accurately determined as long as the H I emission is optically thin. The H I mass does not depend on T's under the optically thin assumption, because the level populations of the

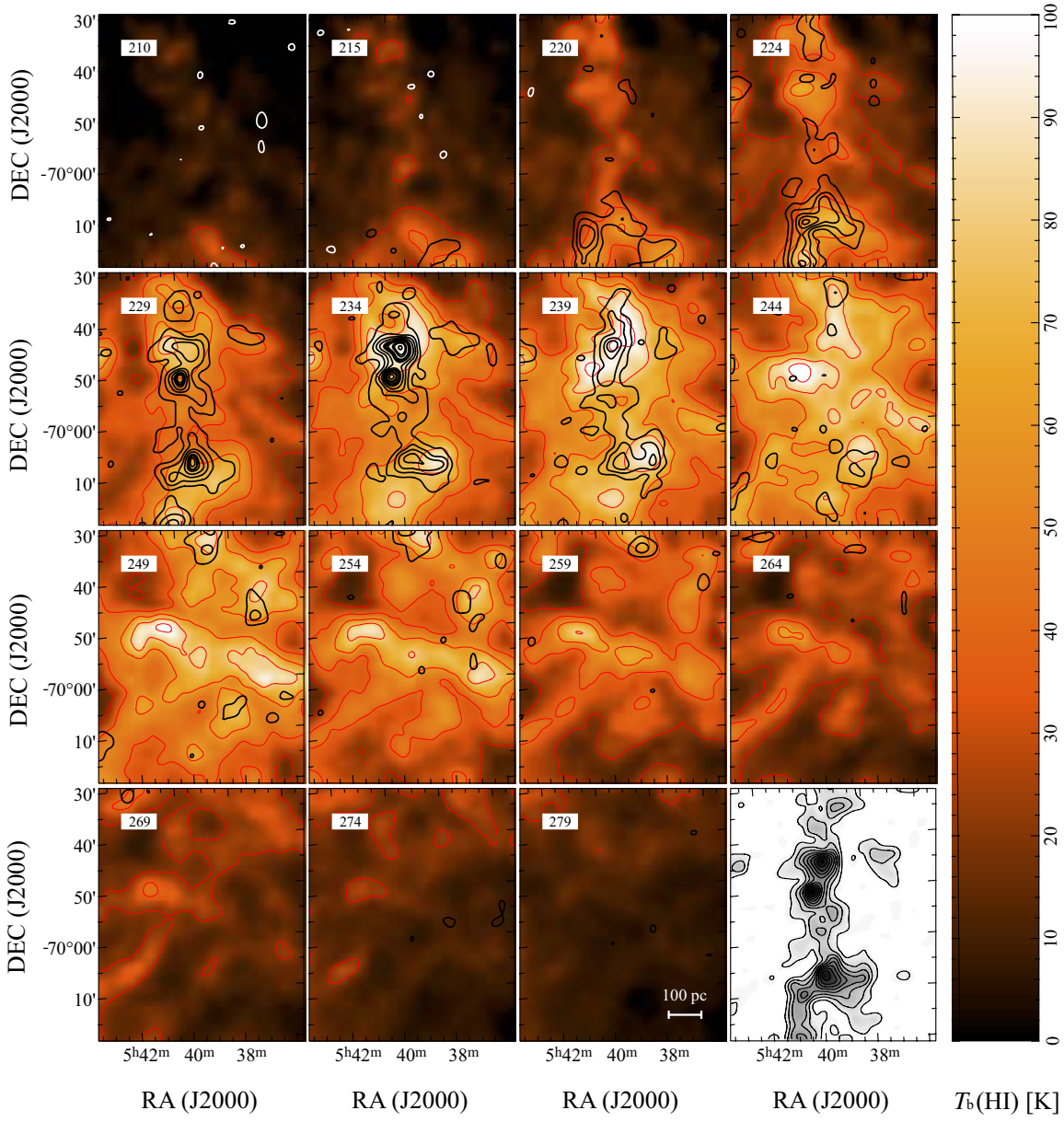

(c)

Figure 5. (Continued)

spin doublet having only $\sim 10^{-5}$ eV is well thermalized in any realistic density range due to the slow magnetic dipole decay in $\sim 10^7$ yr.

Fukui et al. (1999) suggest that the three classes of GMC indicate an evolutionary sequence from Type I to Type III in a few 10 Myr (instead of "Type," these authors used "Class" with the same meaning). Kawamura et al. (2009) present a more detailed analysis of the association between GMCs and young stellar clusters, confirming Fukui et al.'s evolutionary scheme. These studies indicate that only the youngest star clusters with an age less than $\sim$10 Myr are clearly associated with GMCs, and that older clusters with an age greater than 10 Myr are not associated with GMCs. Assuming a steady state scenario, this implies that the natal gas of clusters is quickly disrupted within 10 Myr. Considering the complete sampling of both clusters and GMCs in the LMC, this strongly suggests that the population of Type III GMCs must be replenished on timescales of 10 Myr. Since the typical timescale of GMC formation is at least 10 Myr, as estimated by the crossing timescale—i.e., the cloud size divided by its velocity dispersion, 100 pc/10 km s^{-1} = 10 Myr, a measure of the minimum timescale for GMC formation—we expect to have a similar population of Type III GMCs and Type III precursors. A straightforward interpretation is that Type I and Type II GMCs are these precursors (see for details Kawamura et al. 2009). An alternative possibility is a more ad hoc situation in which Type III GMCs are formed suddenly in a few Myr by an external disturbance, such as a dynamical interaction. Such a strongly time-dependent scenario seems unlikely, however, since the three GMC types are fairly uniformly distributed over the LMC (Kawamura et al. 2009). Figure 4 also shows that the three classes of GMCs are distributed across the galaxy.

We have also seen that Type III GMC tend to be more massive than Type I and Type II GMCs (Table 2; Kawamura et al. 2009). A natural interpretation within the evolutionary scenario is that

Table 2
List of Selected 123 GMCs

Number[a]	Name[a]	Type[b]	Peak Position (CO)[c]		R (CO)[a]	Peak Position (H I)[c]		R(H I)[d]	N (H I)[e]	$\sqrt{\Delta\alpha^2+\Delta\delta^2}$[f]	Comment[g]
			$\alpha(B1950)$	$\delta(B1950)$	(pc)	$\alpha(B1950)$	$\delta(B1950)$	(pc)	10^{21} (cm^{-2})	(pc)	
1	LMC N J0447-6910	I	$4^h47^m.7$	$-69°14'$	44	$4^h47^m.7$	$-69°14'$	34	2.6	0	
4	LMC N J0449-6910	III	$4^h49^m.1$	$-69°16'$	72	$4^h49^m.5$	$-69°14'$	74	2.7	91	
5	LMC N J0449-6826	II	$4^h49^m.5$	$-68°28'$	100	$4^h50^m.1$	$-68°32'$	77	1.7	152	
9	LMC N J0450-6930	II	$4^h50^m.5$	$-69°36'$	33	$4^h50^m.2$	$-69°34'$	55	2.1	83	
11	LMC N J0451-6858	I	$4^h51^m.3$	$-69°4'$	29	$4^h51^m.3$	$-69°4'$	29	2.7	0	
12	LMC N J0451-6704	III	$4^h51^m.9$	$-67°8'$	108	$4^h52^m.2$	$-67°8'$	62	3.2	70	
17	LMC N J0453-6909	III	$4^h54^m.1$	$-69°14'$	85	$4^h53^m.3$	$-69°12'$	59	2.1	159	
22	LMC N J0455-6830	II	$4^h55^m.9$	$-68°36'$	47	$4^h55^m.9$	$-68°36'$	18	2.2	0	
23	LMC N J0455-6634	III	$4^h56^m.4$	$-66°42'$	64	$4^h56^m.4$	$-66°40'$	*	1.9	28	30,32,33,236
24	LMC N J0455-6930	III	$4^h56^m.3$	$-69°36'$	29	$4^h56^m.3$	$-69°36'$	18	0.8	0	
26	LMC N J0457-6844	III	$4^h57^m.5$	$-68°48'$	29	$4^h57^m.5$	$-68°48'$	24	1.5	0	
27	LMC N J0457-6826	III	$4^h57^m.4$	$-68°30'$	40	$4^h57^m.1$	$-68°32'$	18	1.1	91	
35	LMC N J0459-6614	II	$4^h58^m.8$	$-66°18'$	79	$4^h58^m.4$	$-66°24'$	85	2.7	130	30,32,33,236
36	LMC N J0500-6622	II	$5^h0^m.7$	$-66°26'$	52	$5^h0^m.7$	$-66°26'$	37	1.5	0	
38	LMC N J0502-6903	II	$5^h2^m.4$	$-69°6'$	37	$5^h2^m.4$	$-69°6'$	41	2.1	0	
39	LMC N J0503-6553	II	5^h3^m	$-65°58'$	40	5^h3^m	$-65°58'$	62	2.7	0	
40	LMC N J0503-6540	II	$5^h3^m.1$	$-65°44'$	37	$5^h3^m.4$	$-65°46'$	24	0.6	75	
41	LMC N J0503-6828	II	$5^h3^m.6$	$-68°32'$	33	$5^h4^m.3$	$-68°36'$	37	1.1	160	
43	LMC N J0503-6643	II	$5^h3^m.4$	$-66°48'$	33	$5^h3^m.4$	$-66°50'$	24	1.2	26	
45	LMC N J0503-6719	III	$5^h3^m.7$	$-67°24'$	44	$5^h3^m.7$	$-67°24'$	24	2.0	0	
46	LMC N J0504-6802	III	$5^h4^m.6$	$-68°6'$	47	$5^h4^m.3$	$-68°8'$	18	1.0	83	
48	LMC N J0504-7007	II	5^h5^m	$-70°12'$	44	$5^h5^m.1$	$-70°12'$	8	1.4	0	
49	LMC N J0504-7056	III	$5^h5^m.3$	$-71°0'$	52	$5^h5^m.3$	$-71°0'$	34	1.0	0	
52	LMC N J0506-6753	II	$5^h6^m.8$	$-67°58'$	23	$5^h7^m.2$	$-67°56'$	24	1.0	83	
53	LMC N J0507-7041	II	$5^h7^m.9$	$-70°46'$	23	$5^h7^m.8$	$-70°48'$	24	0.9	28	
55	LMC N J0507-6858	I	$5^h8^m.1$	$-69°2'$	47	$5^h8^m.1$	$-69°0'$	29	1.3	28	
57	LMC N J0508-6905	I	$5^h9^m.1$	$-69°8'$	23	$5^h9^m.2$	$-60°8'$	8	1.0	0	
60	LMC N J0509-6827	II	$5^h9^m.4$	$-68°32'$	33	$5^h9^m.5$	$-68°30'$	47	1.6	26	
61	LMC N J0509-7049	II	$5^h10^m.2$	$-70°54'$	29	$5^h9^m.8$	$-70°54'$	8	1.0	87	
62	LMC N J0509-6912	I	$5^h10^m.2$	$-69°16'$	52	$5^h10^m.6$	$-69°16'$	37	1.7	79	
63	LMC N J0510-6853	III	$5^h10^m.4$	$-68°56'$	84	5^h10^m	$-68°52'$	77	2.3	93	245,68
64	LMC N J0510-6706	II	$5^h10^m.7$	$-67°12'$	52	$5^h11^m.1$	$-66°58'$	74	1.2	222	67
65	LMC N J0511-6927	II	$5^h11^m.6$	$-69°30'$	23	5^h12^m	$-69°32'$	47	0.8	83	244,71
67	LMC N J0512-6710	II	$5^h12^m.1$	$-67°14'$	55	$5^h12^m.4$	$-67°14'$	55	1.6	79	64
68	LMC N J0512-6903	II	$5^h12^m.2$	$-69°4'$	80	$5^h11^m.4$	$-69°4'$	88	1.8	166	63
69	LMC N J0512-7028	II	$5^h12^m.8$	$-70°32'$	68	$5^h12^m.8$	$-70°30'$	50	1.5	26	
71	LMC N J0513-6936	II	$5^h13^m.5$	$-69°40'$	79	$5^h13^m.5$	$-69°44'$	59	1.9	62	
72	LMC N J0513-6922	III	$5^h13^m.5$	$-69°26'$	49	$5^h13^m.2$	$-69°24'$	34	1.7	83	
74	LMC N J0514-7010	II	$5^h14^m.9$	$-70°14'$	66	$5^h14^m.9$	$-70°14'$	34	1.6	0	
77	LMC N J0515-7034	I	$5^h15^m.6$	$-70°38'$	44	$5^h15^m.6$	$-70°38'$	18	0.6	0	
80	LMC N J0516-6807	II	$5^h16^m.1$	$-68°2'$	124	$5^h17^m.2$	$-68°4'$	62	1.4	237	
81	LMC N J0516-6616	I	5^h16^m	$-66°20'$	29	5^h16^m	$-66°18'$	24	0.3	26	
83	LMC N J0516-6922	II	5^h17^m	$-69°26'$	23	$5^h17^m.4$	$-69°26'$	34	1.3	87	91
84	LMC N J0516-6559	II	$5^h16^m.7$	$-66°2'$	29	$5^h17^m.1$	$-66°2'$	29	0.6	70	
86	LMC N J0517-7114	III	$5^h18^m.3$	$-71°18'$	44	$5^h18^m.3$	$-71°20'$	37	1.3	26	
89	LMC N J0517-6642	II	$5^h17^m.6$	$-66°44'$	40	$5^h17^m.6$	$-66°44'$	18	0.9	0	
90	LMC N J0517-6932	II	$5^h18^m.5$	$-69°36'$	33	$5^h18^m.5$	$-69°36'$	*	0.9	0	
92	LMC N J0518-7001	I	$5^h18^m.8$	$-70°6'$	33	$5^h18^m.1$	$-70°4'$	18	1.1	168	
93	LMC N J0518-6620	I	$5^h18^m.3$	$-66°24'$	23	5^h18^m	$-66°22'$	*	0.5	75	
94	LMC N J0518-6951	II	$5^h19^m.2$	$-69°54'$	23	$5^h19^m.2$	$-69°56'$	24	0.9	26	
95	LMC N J0519-6625	I	5^h19^m	$-66°28'$	23	5^h19^m	$-66°30'$	*	1.2	26	100
96	LMC N J0519-6938	III	$5^h19^m.6$	$-69°40'$	72	$5^h19^m.6$	$-69°40'$	29	2.0	0	
97	LMC N J0519-7113	I	5^h20^m	$-71°18'$	40	$5^h20^m.4$	$-71°16'$	24	0.9	91	
99	LMC N J0520-7043	I	$5^h20^m.4$	$-70°44'$	52	5^h20^m	$-70°46'$	37	1.0	91	
100	LMC N J0520-665	II	5^h20^m	$-66°54'$	37	5^h21^m	$-66°50'$	52	1.3	226	
103	LMC N J0521-714	II	$5^h21^m.7$	$-71°46'$	23	$5^h21^m.7$	$-71°46'$	24	1.2	0	
104	LMC N J0521-701	II	$5^h21^m.6$	$-70°16'$	49	$5^h21^m.2$	$-70°18'$	29	0.8	91	
105	LMC N J0521-700	II	$5^h21^m.6$	$-70°4'$	79	$5^h21^m.6$	$-70°6'$	44	1.4	26	
106	LMC N J0521-684	II	$5^h21^m.5$	$-68°44'$	29	$5^h21^m.5$	$-68°44'$	8	1.7	0	
108	LMC N J0521-684	II	$5^h21^m.8$	$-68°50'$	55	$5^h21^m.8$	$-68°50'$	34	1.4	0	
110	LMC N J0522-694	III	$5^h22^m.7$	$-69°44'$	52	$5^h22^m.3$	$-69°44'$	18	1.2	79	
115	LMC N J0522-654	III	$5^h22^m.6$	$-65°44'$	57	$5^h22^m.6$	$-65°42'$	44	1.7	26	
118	LMC N J0523-682	I	$5^h22^m.9$	$-68°24'$	44	$5^h22^m.9$	$-68°26'$	37	3.2	26	
119	LMC N J0523-664	II	5^h23^m	$-66°46'$	57	$5^h22^m.7$	$-66°46'$	41	2.5	79	
123	LMC N J0523-713	II	$5^h24^m.2$	$-71°42'$	49	$5^h26^m.4$	$-71°38'$	62	1.4	466	131,249
126	LMC N J0524-672	II	$5^h24^m.5$	$-67°30'$	44	$5^h24^m.5$	$-67°30'$	24	2.3	0	

Table 2
(Continued)

Number[a]	Name[a]	Type[b]	Peak Position (CO)[c]		R (CO)[a]	Peak Position (H I)[c]		R(H I)[d]	N (H I)[e]	$\sqrt{\Delta\alpha^2+\Delta\delta^2}$[f]	Comment[g]
			$\alpha(B1950)$	$\delta(B1950)$	(pc)	$\alpha(B1950)$	$\delta(B1950)$	(pc)	10^{21} (cm^{-2})	(pc)	
127	LMC N J0524-702	I	$5^h24^m.8$	$-70°30'$	37	$5^h24^m.4$	$-70°30'$	24	0.6	87	
130	LMC N J0524-691	II	$5^h24^m.9$	$-69°18'$	33	$5^h24^m.5$	$-69°12'$	47	1.2	123	
131	LMC N J0524-713	II	$5^h25^m.5$	$-71°36'$	29	$5^h25^m.9$	$-71°38'$	64	1.7	99	123,249
132	LMC N J0525-694	II	$5^h26^m.2$	$-69°52'$	33	$5^h25^m.8$	$-69°56'$	34	1.0	99	
133	LMC N J0525-691	III	5^h26^m	$-69°20'$	33	$5^h24^m.5$	$-69°12'$	47	0.8	359	130
134	LMC N J0525-662	II	$5^h25^m.7$	$-66°24'$	23	$5^h25^m.3$	$-66°26'$	116	3.8	75	135
136	LMC N J0526-683	II	$5^h26^m.2$	$-68°38'$	37	$5^h26^m.2$	$-68°38'$	41	1.4	0	
139	LMC N J0526-684	III	$5^h26^m.6$	$-68°50'$	29	$5^h26^m.3$	$-68°48'$	29	1.9	91	
141	LMC N J0526-655	II	$5^h26^m.5$	$-65°56'$	23	$5^h26^m.2$	$-66°0'$	160	2.0	93	134,135,250
143	LMC N J0526-711	II	$5^h27^m.5$	$-71°22'$	97	5^h26^m	$-71°26'$	120	1.3	346	153,156
145	LMC N J0527-703	II	5^h28^m	$-70°38'$	40	$5^h28^m.1$	$-70°40'$	18	0.6	26	
146	LMC N J0527-705	II	$5^h28^m.6$	$-70°54'$	37	$5^h28^m.6$	$-70°54'$	72	1.0	0	149
149	LMC N J0528-705	II	5h29m	$-71°0'$	33	$5^h29^m.4$	$-71°0'$	24	1.7	87	
150	LMC N J0529-683	II	$5^h30^m.2$	$-68°32'$	29	$5^h30^m.6$	$-68°36'$	142	1.8	106	154,163
153	LMC N J0530-710	III	$5^h31^m.6$	$-71°10'$	80	$5^h31^m.6$	$-71°10'$	47	2.6	0	
154	LMC N J0531-683	III	$5^h31^m.7$	$-68°34'$	108	$5^h32^m.7$	$-68°28'$	55	2.7	243	150,163
155	LMC N J0532-674	III	5^h32^m	$-67°46'$	68	$5^h32^m.7$	$-67°46'$	44	3.1	157	
156	LMC N J0532-711	II	$5^h32^m.9$	$-71°16'$	47	$5^h32^m.9$	$-71°16'$	41	2.5	0	
157	LMC N J0532-683	II	$5^h32^m.5$	$-68°40'$	40	$5^h32^m.5$	$-68°40'$	41	2.7	0	
158	LMC N J0532-662	III	$5^h32^m.4$	$-66°30'$	47	5^h32^m	$-66°26'$	29	0.9	99	
162	LMC N J0532-685	II	$5^h33^m.4$	$-69°0'$	33	5^h33^m	$-69°0'$	18	2.4	79	
171	LMC N J0535-690	III	5^h36^m	$-69°4'$	66	$5^h36^m.4$	$-69°4'$	91	3.5	79	183
172	LMC N J0535-684	II	$5^h36^m.2$	$-68°46'$	37	$5^h35^m.8$	$-68°46'$	41	1.6	79	
179	LMC N J0537-661	III	$5^h37^m.3$	$-66°20'$	47	$5^h37^m.3$	$-66°20'$	44	2.1	0	
180	LMC N J0537-662	II	$5^h37^m.4$	$-66°28'$	23	$5^h37^m.1$	$-66°30'$	34	1.8	75	
184	LMC N J0538-693	II	$5^h38^m.7$	$-69°36'$	33	$5^h39^m.1$	$-69°34'$	41	3.5	83	191
190	LMC N J0538-685	III	$5^h38^m.9$	$-68°56'$	23	$5^h41^m.1$	$-68°54'$	81	2.9	480	
191	LMC N J0539-693	III	$5^h39^m.4$	$-69°32'$	57	$5^h39^m.1$	$-69°34'$	41	3.5	83	184
205	LMC N J0542-711	III	$5^h42^m.1$	$-71°20'$	64	5^h42^m	$-71°18'$	47	2.5	28	
207	LMC N J0542-694	II	$5^h43^m.5$	$-69°46'$	23	$5^h43^m.5$	$-69°46'$	18	4.1	0	266
208	LMC N J0543-675	III	$5^h43^m.5$	$-67°58'$	37	$5^h43^m.8$	$-67°58'$	34	2.0	79	211
209	LMC N J0543-692	II	$5^h43^m.9$	$-69°28'$	33	$5^h44^m.2$	$-69°22'$	47	3.0	106	214,216,268
211	LMC N J0543-675	III	$5^h43^m.8$	$-67°56'$	23	$5^h43^m.8$	$-67°58'$	29	1.8	28	208
214	LMC N J0543-691	II	$5^h43^m.4$	$-69°16'$	33	$5^h44^m.2$	$-69°22'$	44	2.5	211	209,216,268
215	LMC N J0544-712	I	$5^h45^m.2$	$-71°28'$	59	$5^h44^m.7$	$-71°28'$	57	1.9	87	
218	LMC N J0544-671	II	$5^h44^m.9$	$-67°20'$	29	$5^h44^m.4$	$-67°28'$	50	1.0	167	213
220	LMC N J0545-694	III	$5^h45^m.9$	$-69°50'$	47	$5^h45^m.6$	$-69°52'$	37	2.0	83	
222	LMC N J0546-710	I	$5^h46^m.8$	$-71°6'$	44	$5^h46^m.8$	$-71°6'$	44	1.7	0	
223	LMC N J0546-693	II	$5^h46^m.8$	$-69°38'$	52	$5^h47^m.2$	$-69°40'$	57	3.3	99	
224	LMC N J0547-680	I	$5^h47^m.6$	$-68°10'$	33	5^h48^m	$-68°10'$	55	1.7	79	
225	LMC N J0547-704	I	$5^h47^m.8$	$-70°42'$	87	$5^h47^m.8$	$-70°40'$	*	1.3	28	228
226	LMC N J0547-6953	II	$5^h48^m.7$	$-69°54'$	61	5^h48^m	$-69°56'$	104	1.6	159	223,227,270
230	LMC N J0555-681	III	$5^h55^m.9$	$-68°10'$	73	$5^h55^m.9$	$-68°10'$	*	1.3	0	271
231	LMC N J0447-672	I	$4^h47^m.2$	$-67°34'$	17	$4^h47^m.1$	$-67°36'$	190	1.2	28	2,232
232	LMC N J0448-672	I	4^h48^m	$-67°28'$	17	$4^h47^m.2$	$-67°18'$	82	1.2	229	2
233	LMC N J0449-681	II	$4^h49^m.8$	$-68°16'$	17	$4^h49^m.5$	$-68°12'$	88	1.3	86	6
236	LMC N J0458-661	II	$4^h58^m.7$	$-66°22'$	17	$4^h58^m.4$	$-66°24'$	75	3.7	83	30,32,33,35
237	LMC N J0459-660	II	$4^h59^m.8$	$-66°12'$	17	$5^h0^m.2$	$-66°12'$	*	2.7	70	
243	LMC N J0511-705	I	$5^h12^m.3$	$-70°54'$	17	$5^h12^m.7$	$-70°54'$	8	0.7	87	
244	LMC N J0511-692	II	5^h12^m	$-69°32'$	17	5^h12^m	$-69°32'$	29	1.1	0	65
247	LMC N J0521-673	I	$5^h21^m.8$	$-67°42'$	17	$5^h22^m.1$	$-67°36'$	34	0.9	117	
252	LMC N J0528-672	III	5^h28^m	$-67°28'$	17	5^h28^m	$-67°28'$	29	2.3	0	
253	LMC N J0530-675	I	$5^h30^m.7$	$-68°0'$	17	5^h31^m	$-67°58'$	47	2.1	83	
258	LMC N J0535-661	II	$5^h35^m.3$	$-66°20'$	17	$5^h35^m.3$	$-66°18'$	24	0.7	28	
266	LMC N J0543-694	II	$5^h43^m.6$	$-69°48'$	17	$5^h43^m.5$	$-69°46'$	18	3.6	28	207
270	LMC N J0547-695	II	$5^h48^m.1$	$-70°0'$	17	$5^h48^m.6$	$-70°6'$	82	2.0	143	226,227
271	LMC N J0553-682	I	$5^h53^m.3$	$-68°24'$	17	$5^h53^m.3$	$-68°24'$	55	1.9	0	

Notes.

[a] Fukui et al. (2008).

[b] Kawamura et al. (2009).

[c] Position of peak integrated intensity. Data are from Fukui et al. (2008).

[d] H I cloud radius defined as $R = \sqrt{\frac{S}{\pi}}$. Here S is the cloud area, calculated by summing the areas of all pixels detected above 80% of the peak integrated intensity level. Asterisks show H I clouds whose extent is poorly defined.

[e] H I column density of position at peak integrated intensity estimated by using the relation: $N(\mathrm{H\,I})\ [\mathrm{cm^{-2}}] = 1.82 \times 10^{18} \int T_b(\mathrm{H\,I})\, dv\ [\mathrm{K\ km\ s^{-1}}]$).

[f] Difference between CO peak position and H I peak position: (CO(α, δ) − H I(α, δ)).

[g] H I clouds including two or more GMCs: the numbers show GMCs that are located in the same H I cloud.

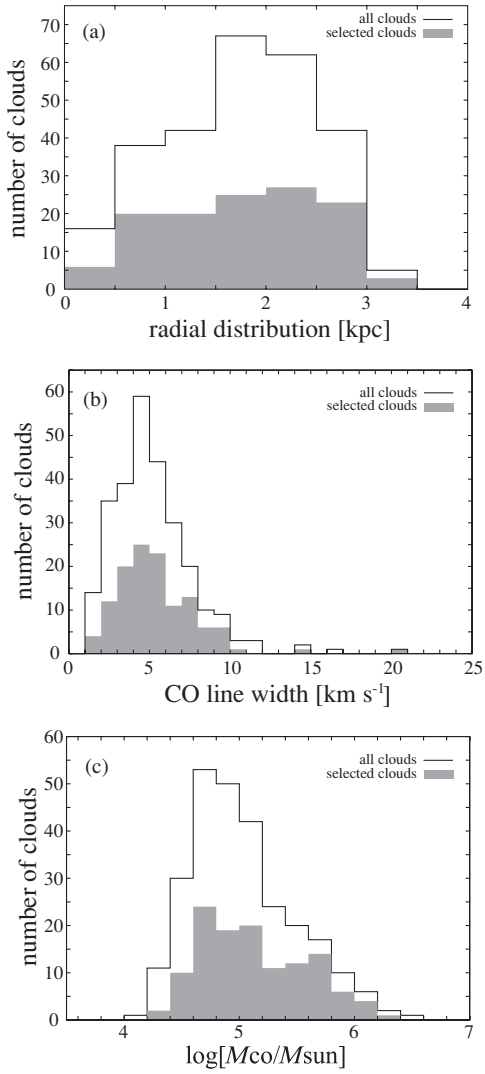

Figure 6. Histograms of three parameters: (a) the distance from the kinematic center of the galaxy (kpc), (b) the CO line width (km s^{-1}), and (c) the CO cloud mass ($M_{\odot}$) for the 123 GMCs used in our analysis. The solid lines show the distribution of these properties for all the clouds in the Fukui et al. (2008) catalog; the gray shaded regions represent the distribution for the 123 selected GMCs (see also Table 2).

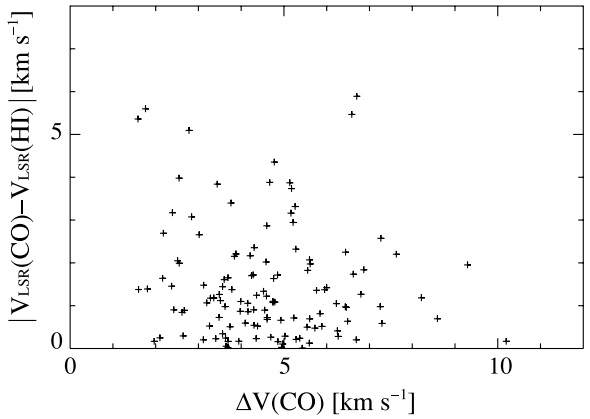

Figure 7. Absolute difference between the central velocity of the H I and CO emission, $|V_{LSR}(CO) - V_{LSR}(H\,I)|$, vs. the CO line width, ΔV (CO) for the 123 GMCs in our sample. The dotted line shows $|V_{LSR}(CO) - V_{LSR}(H\,I)| = \Delta V(CO)$.

the enveloping H I gas accretes onto a GMC and that the GMC mass increases with time. The accreted H I envelope is converted

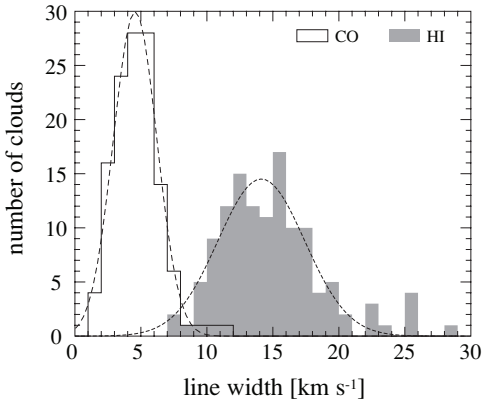

Figure 8. Histogram of the CO and H I line widths toward the position of the CO peak position for the 123 selected GMCs. The dotted lines show Gaussian fits to the histograms. The mean values (standard derivations) for the CO and H I distributions are 4.6 (1.6) and 14.1 (3.3) km s^{-1}, respectively.

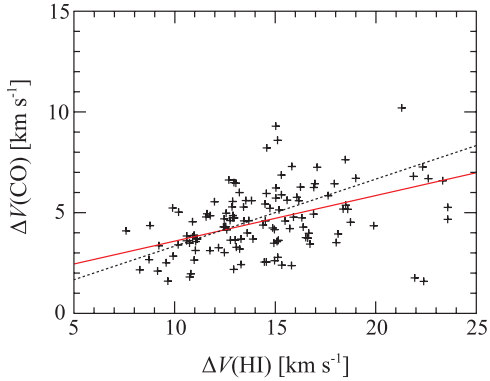

Figure 9. Plot of the CO vs. H I line width for the 123 GMCs in our sample. The red line is the regression line $\Delta V(CO) = (1.32 \pm 0.04) + (0.23 \pm 0.003)\Delta V(H\,I)$, and the dotted line shows $\Delta V(H\,I) = 3 \times \Delta V(CO)$. The Spearman rank correlation coefficient is 0.39.

(A color version of this figure is available in the online journal.)

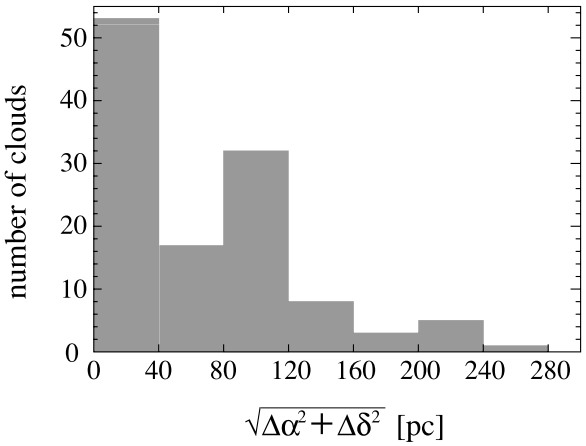

Figure 10. Histogram of the projected separation between the CO and H I peak positions, as listed in Table 2. The separation between the CO and H I peak positions for four of the 123 clouds is greater than 300 pc; these clouds are not shown.

into H_2 in ~10 Myr due to increased density, optical extinction, and UV shielding. This infall scenario is consistent with the linear relationship between $I(H\,I)$ and $I(CO)$ in Figure 12; by contrast, growth of GMCs via collisions between H I clouds would have a steeper relationship, with $I(CO)$ proportional to $I(H\,I)^2$. For an infall scenario, the infall motion can arise from the

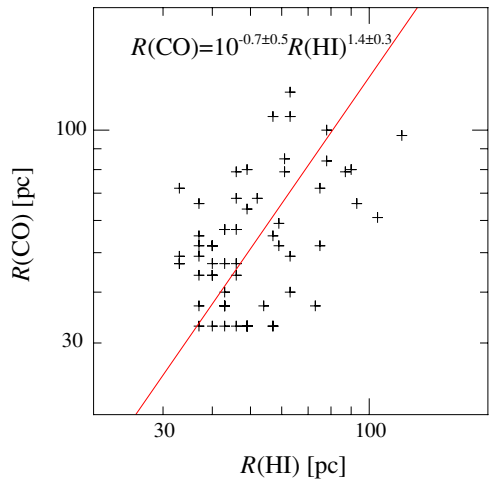

Figure 11. Radius of the GMC, R(CO), vs. the radius of the H I envelope, R(H I), for the 62 clouds with radii greater than 30 pc, as listed in Table 2. The red line is the regression line $R(\mathrm{CO}) = 10^{-0.7\pm0.5} R(\mathrm{H\,I})^{1.4\pm0.3}$; the Spearman rank correlation coefficient is 0.45.

(A color version of this figure is available in the online journal.)

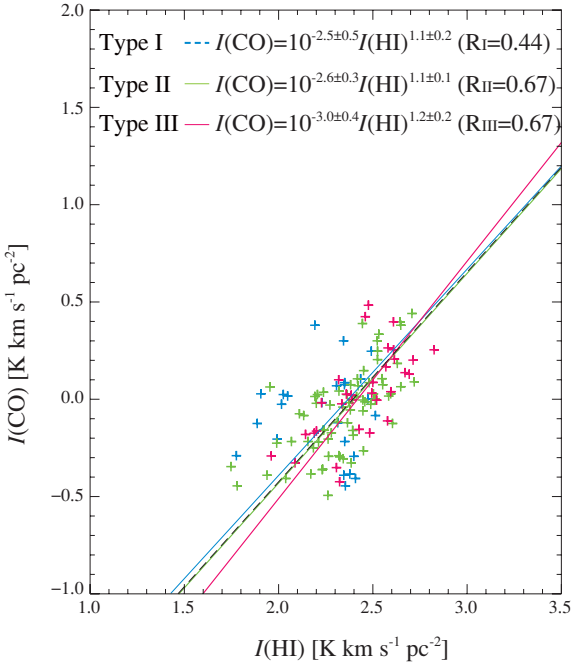

Figure 12. CO vs. H I integrated intensity for the 123 clouds in our sample, averaged over the projected area of each GMC or H I envelope. Blue, green, and red plot symbols represent Type I, Type II, and Type III GMCs, respectively. The black dotted line shows the regression line for all the 123 clouds; $I(\mathrm{CO}) = 10^{-2.6\pm0.2} I(\mathrm{H\,I})^{1.1\pm0.1}$. The regression lines and Spearman rank correlation coefficients (R_{I}, R_{II}, and R_{III}) for the three GMC types are shown at the top of the plot.

(A color version of this figure is available in the online journal.)

gravity of a GMC and possibly from a converging flow driven by super bubbles, while the thermal motion is negligibly small 1.4–3 km s^{-1} for kinetic temperatures of ∼150–600 K. We can roughly estimate the infall velocity to be half of the H I line width, i.e., ∼7 km s^{-1}. This value is consistent with the free-fall velocity, ∼6 km s^{-1}, for a typical Type II GMC. For spherical accretion, where the GMC is surrounded by an H I envelope with a radius of ∼40 pc, volume density of n(H I) ∼10 cm^{-3}, and an infall speed of ∼7 km s^{-1}, we estimate the mass accretion rate to be ∼0.05 $M_{\odot}$ yr^{-1}. Over the typical timescale of the GMC evolution, i.e., ∼10 Myr, the increase in molecular mass amounts

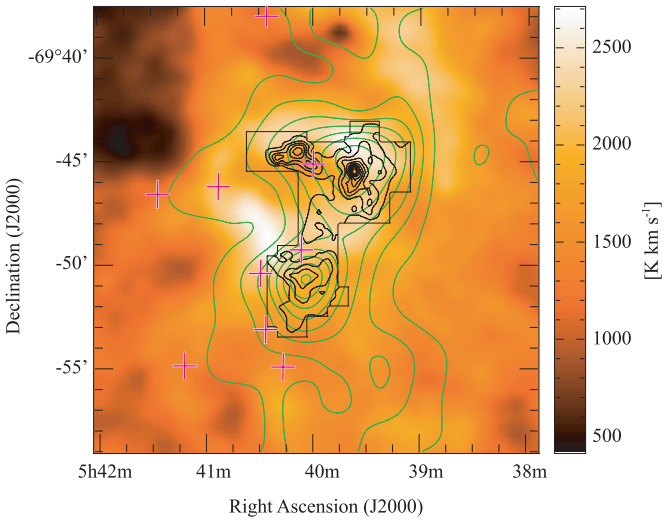

Figure 13. CO and H I emission in the N159 region. The gray-scale image represents the combined ATCA+Parkes H I integrated intensity data (Kim et al. 2003). The black contours are integrated CO (J = 3–2) emission by ASTE (Minamidani et al. 2008) and green contours are integrated CO (J = 1–0) emission by NANTEN (Fukui et al. 2008). For CO (J = 3–2), the contour levels are from 5 K km s^{-1} in 10 K km s^{-1} intervals; for CO (J = 1–0), the contours levels are from 1.2 K km s^{-1} in steps of 2.4 K km s^{-1}. The thin black lines indicate the region observed in CO (J = 3–2) emission by ASTE. The crosses indicate the positions of H II regions cataloged by Davies et al. (1976).

(A color version of this figure is available in the online journal.)

to ∼5 × 10^5 $M_{\odot}$, which is roughly consistent with the observed typical value for the mass of a Type III GMC (∼4 × 10^5 $M_{\odot}$, Table 1). In the evolutionary picture, the mass accretion of a GMC is terminated by the violent disruption and/or ionization of the molecular material by stellar winds and ionization from young stars.

The infall scenario offers a reasonable interpretation of the H I and CO properties of GMCs that we have explored in this paper. It remains to be seen, however, if an infall velocity field is consistent with 2D observations; careful analysis of an isolated H I envelope with little kinematical disturbance or nearby contamination could be used to verify this. It is also important to clarify whether the H I line width is affected by turbulence to a significant degree.

It could be argued that the H I gas surrounding GMCs is supplied by the recombination of H II into H I, as both Type II and Type III GMCs are associated with H II regions. This alternative seems unlikely, however: first, the H II regions in Type II GMCs are compact and therefore do not constitute a significant mass reservoir; second, the H I envelope in Type III GMCs are not spatially well matched with the H II regions and clusters. In N159, for instance, the H II regions and young clusters are confined to the north of the GMC, whereas the H I is more widely distributed in the east and south (Figure 13).

4.2. *H I–H$_2$ Conversion in GMCs*

This study has shown that the H I and CO distributions correlate well on 40–100 pc scales. It is worth noting, however, that the correlation becomes less clear on smaller scales of ∼10 pc within a GMC. Figure 13 shows an overlay of the H I and CO distributions for the Type III GMC N159, where the CO data were obtained using the ASTE 10 m submillimeter telescope in the ^{12}CO J = 3–2 emission line (Minamidani et al. 2008). Figure 13 shows that the H I becomes less bright at T_{b}(H I) 70–80 K toward N159E at (R.A., decl.) = ($5^{\mathrm{h}}40^{\mathrm{m}}$, −69°, 45′),

compared to intensities of T_b(H I) ∼120 K in the H I envelope. A similar behavior was noted by Ott et al. (2008). This is unlikely to be caused by absorption of the radio continuum emission, as there is no radio continuum emission toward N 159E. We regard this behavior to be illustrative of the conversion of H I into H_2, as well as the lower spin temperature in the interior of a GMC. In the inner part of a GMC, H I is converted into H_2 via reactions on grain surfaces on a timescale of ∼10 Myr. The H I density is typically ∼1 cm^{-3}, compared to a total molecular density of a few 100 cm^{-3}, corresponding to atomic to molecular hydrogen ratio of ∼100 (e.g., Allen & Robinson 1977; Spitzer 1978; Goldsmith et al. 2007). The spin temperature is also lower, and is likely to equal the molecular gas kinetic temperature of ∼60 K (e.g., Sato & Fukui 1978; Mizuno et al. 2009). In the H I envelope, on the other hand, the spin temperature is probably between ∼150 and 600 K and the H I density is estimated to be ∼10 cm^{-3} with no H_2. The lower T_b(H I) in the interior is likely due to the lower spin temperature and the lower H I density. The mass of the apparently cold H I gas toward N159E is approximately 10% of the mass of the H I envelope, ∼10^5 $M_\odot$, if we assume that the cold H I is optically thin, which suggests that the cold H I within the GMC is not a dominant mass component of the atomic+molecular cloud complex.

It has been shown that there are cold H I components in the LMC as measured from emission and absorption observations toward radio continuum sources (Dickey et al. 1994). These authors detected H I absorption features toward 19 of 30 continuum sources in the LMC and argued that T_s of the cold components can be as low as 40 K. Such cold H I components may be associated with GMCs. It is however not clear observationally how the cold H I in absorption is related to GMCs because none of the absorption measurements by Dickey et al. (1994) coincide with the NANTEN GMCs.

An issue which has been raised in Wong et al. (2009) is that higher H I intensity is a necessary but not sufficient condition for CO formation. In other words, there are many places with high H I intensities in the LMC without CO. The current analysis has focused solely on the H I gas surrounding GMCs and therefore does not directly address this issue. We note, however, that it is possible that H I gas with the same intensity can have a significantly different density. We propose an interpretation that the atomic gas in regions with high H I intensities but no CO may have lower densities and higher temperatures. This interpretation could be tested in the future by high velocity-resolution H I observations that can resolve subtle variations in H I profiles and hence identify spatial variations of the atomic gas temperature.

5. SUMMARY

We have carried out the first 3D analysis of the connection between the CO and H I emission in a galaxy. The major results of our study are as follows.

1. A 3D comparison at a resolution of 40 pc × 40 pc × 1.7 km s^{-1} has revealed that the fraction of H I associated with CO tends to increase as a monotonic function of H I intensity without a sharp threshold for the CO formation.
2. We find that GMCs are associated with H I envelopes on scales of ∼50–100 pc. The H I envelopes have typical volume densities of ∼10 cm^{-3} and an average line width of ∼14 km s^{-1}, which is about three times larger than the line width of CO. We argue that the H I envelopes are gravitationally bound by GMCs.
3. For 123 GMCs with single-peaked H I profiles, we find a correlation such that [average CO intensity] ∝ [average H I intensity]$^{1.1\pm0.1}$. There is a clear increase of the associated H I intensity from GMC Type I to Type III.
4. We interpret our results to mean that a GMC increases in mass via continuous H I accretion over a timescale of ∼10 Myr and with a mass accretion rate of 0.05 $M_\odot$ yr^{-1}, before being disrupted by ionization and stellar winds from young clusters. The accreted H I is likely to be converted to molecular hydrogen due to the higher shielding within a GMC.

The NANTEN project is based on a mutual agreement between Nagoya University and the Carnegie Institution of Washington (CIW). We greatly appreciate the hospitality of all the staff members of the Las Campanas Observatory of CIW. We are thankful to the many Japanese public donors and companies who contributed to the realization of the project. This study has made use of SIMBAD Astronomical Database and NASA's Astrophysics Data System Bibliographic Services. This work is financially supported in part by a Grant-in-Aid for Scientific Research from the Ministry of Education, Culture, Sports, Science and Technology of Japan (No. 15071203), from JSPS (No. 14102003, No. 18684003, No. 20244014, and core-to-core program 17004). N.M. acknowledges the support of the Sumitomo Foundation, and T.O. of the Mitsubishi Foundation.

REFERENCES

Allen, M., & Robinson, G. W. 1977, ApJ, 212, 396
Andersson, B. -G., Wannier, P. G., & Morris, M. 1991, ApJ, 366, 464
Bica, E., Claria, J. J., Dottori, H., Santos, J. F. C., Jr., & Piatti, A. E. 1996, ApJS, 102, 57
Blitz, L., Fukui, Y., Kawamura, A., Leroy, A., Mizuno, N., & Rosolowsky, E. 2007, in Protostars and Planet V, ed. B. Reipurth, D. Jewitt, & K. Keil (Tucson, AZ: Univ. Arizona Press), 951
Davies, R. D., Elliott, K. H., & Meaburn, J. 1976, MmRAS, 81, 89
Dickey, J. M., Mebold, U., Marx, M., Amy, S., Haynes, R. F., & Wilson, W. 1994, A&A, 289, 357
Dobashi, K., Bernard, J. P., Hughes, A., Paradis, D., Reach, W. T., & Kawamura, A. 2008, A&A, 484, 205
Fukui, Y. 2007, in IAU Symp. 237, Triggered Star Formation in a Turbulent ISM, ed. B. Elmegreen & J. Palous (Cambridge: Cambridge Univ. Press), 31
Fukui, Y., et al. 1999, PASJ, 51, 745
Fukui, Y., et al. 2008, ApJS, 178, 56
Goldsmith, P., Li, D., & Krco, M. 2007, ApJ, 654, 273
Hasegawa, T., Sato, F., & Fukui, Y. 1983, AJ, 88, 658
Imara, N., & Blitz, L. 2007, ApJ, 662, 969
Israel, F. P., Maloney, P. R., Geis, N., Herrmann, F., Madden, S. C., Poglitsch, A., & Stacey, G. J. 1996, ApJ, 465, 738
Kawamura, A., et al. 2009, ApJS, 184, 1
Kennicutt, R. C., Jr. 1998, ApJ, 498, 541
Kim, S., Dopita, M. A., Staveley-Smith, L., & Bessel, M. S. 1999, AJ, 118, 2797
Kim, S., Staveley-Smith, L., Dopita, M. A., Sault, R. J., Freeman, K. C., Lee, Y., & Chu, Y.-H. 2003, ApJ, 148, 473
Minamidani, T., et al. 2008, ApJS, 175, 485
Mizuno, N., Muller, E., Maeda, H., Kawamura, A., Minamidani, T., Onishi, T., Mizuno, A., & Fukui, Y. 2006, ApJ, 643, 107
Mizuno, N., Rubio, M., Mizuno, A., Yamaguchi, R., Onishi, T., & Fukui, Y. 2001, PASJ, 53, L45
Mizuno, Y., et al. 2009, PASJ, submitted
Ott, J., et al. 2008, PASA, 25, 129
Sato, F., & Fukui, Y. 1978, AJ, 83, 1607
Schmidt, Th. 1972, A&A, 16, 95
Spitzer, L., Jr. 1978, Physical Processes in the Interstellar Medium (New York: Wiley Interscience)
Wannier, P. G., Lichten, S. M., & Morris, M. 1983, ApJ, 268, 727
Wong, T., et al. 2009, ApJ, 696, 370 (Paper I)
Yamaguchi, R., et al. 2001, PASJ, 53, 9